# Immersion mode ice nucleation measurements with the new Portable Immersion Mode Cooling chAmber (PIMCA)

**Monika Kohn[1], Ulrike Lohmann[1], André Welti[1,2], and Zamin A. Kanji[1]**

[1]Institute for Atmospheric and Climate Science, ETH Zurich, Zurich, Switzerland, [2]Now at Leibniz-Institute for Tropospheric Research, TROPOS, Leipzig, Germany

**Correspondence to:**
Z. A. Kanji and M. Kohn,
zamin.kanji@env.ethz.ch;
monika.kohn@env.ethz.ch

**Abstract** The new Portable Immersion Mode Cooling chAmber (PIMCA) has been developed for online immersion freezing of single-immersed aerosol particles. PIMCA is a vertical extension of the established Portable Ice Nucleation Chamber (PINC). PIMCA immerses aerosol particles into cloud droplets before they enter PINC. Immersion freezing experiments on cloud droplets with a radius of 5–7 μm at a prescribed supercooled temperature ($T$) and water saturation can be conducted, while other ice nucleation mechanisms (deposition, condensation, and contact mode) are excluded. Validation experiments on reference aerosol (kaolinite, ammonium sulfate, and ammonium nitrate) showed good agreement with theory and literature. The PIMCA-PINC setup was tested in the field during the Zurich AMBient Immersion freezing Study (ZAMBIS) in spring 2014 in Zurich, Switzerland. Significant concentrations of submicron ambient aerosol triggering immersion freezing at $T > 236$ K were rare. The mean frozen cloud droplet number concentration was estimated to be $7.22 \cdot 10^5$ L$^{-1}$ for $T < 238$ K and determined from the measured frozen fraction and cloud condensation nuclei (CCN) concentrations predicted for the site at a typical supersaturation of SS = 0.3%. This value should be considered as an upper limit of cloud droplet freezing via immersion and homogeneous freezing processes. The predicted ice nucleating particle (INP) concentration based on measured total aerosol larger than 0.5 μm and the parameterization by DeMott et al. (2010) at $T = 238$ K is INP$_{D10} = 54 \pm 39$ L$^{-1}$. This is a lower limit as supermicron particles were not sampled with PIMCA-PINC during ZAMBIS.

## 1. Introduction

The Earth's energy and radiation budget is strongly coupled to the presence of clouds, which influence the hydrological cycle by transporting water and are necessary for the formation of precipitation in the atmosphere. Hydrometeors like cloud droplets and, in particular, ice crystals which are found in cirrus and mixed-phase clouds influence the radiative budget by reflecting incoming solar radiation back to space and by absorbing outgoing (terrestrial) radiation from the Earth's surface. These effects can lead to a cooling or warming of the atmosphere. The formation of primary ice crystals (ice nucleation) can significantly change the cloud physical properties. The ice phase in clouds is relevant for initiating precipitation and affects cloud cover and lifetime [*DeMott et al.*, 2010; *Lohmann and Feichter*, 2005]. It is important to understand the processes leading to ice formation in the atmosphere to appropriately include them into global circulation models (GCMs).

Ice nucleation can take place in the atmosphere via different pathways. Homogeneous freezing occurs at temperatures below 235 K [*Pruppacher and Klett*, 1997]. Heterogeneous nucleation can take place where an aerosol particle called ice nucleating particle (INP) provides a surface for ice to nucleate upon, leading to ice formation at smaller supersaturation with respect to ice and supercooling ($T > 235$ K) than is required for homogeneous freezing [*Vali et al.*, 2015]. Although homogeneous ice nucleation can be very active at low temperatures prevailing at high altitudes, the dominance of homogeneous freezing has been questioned recently by *Cziczo et al.* [2013] who found indications for heterogeneous ice nucleation at cirrus cloud conditions. Heterogeneous ice nucleation can occur via four mechanisms, where different phases of water are involved. Mechanisms are summarized in *Vali* [1985], and later, with more specific distinctions by *Vali et al.* [2015]. In summary, deposition nucleation occurs when water vapor directly deposits on an INP and forms an ice crystal without an intermediate liquid phase being involved. Immersion freezing occurs when an INP immersed in a supercooled droplet initiates freezing upon sufficient supercooling, while condensation freezing takes place when water vapor condenses on a supercooled INP followed by freezing during or immediately

after the condensation process. Lastly, contact freezing can occur when a supercooled cloud droplet collides with an INP. Recently, the distinction between the freezing modes has been challenged by some studies. *Marcolli* [2014] hypothesized that deposition nucleation may in fact be immersion freezing of trapped water in voids and cavities at subsaturated conditions with respect to water, which implies a pore condensation and freezing mechanism rather than deposition nucleation on the particle surface.

The ice nucleation activity depends on the physical and chemical properties of the aerosol particles, with insolubility, size, chemical bonding, active sites, and crystallographic structures being potential requirements [*Pruppacher and Klett*, 1997]. This knowledge has been challenged in the past, for example, by observation that crystalline ammonium sulfate acts as deposition mode INP [*Abbatt et al.*, 2006] or glassy aerosols as immersion INP [*Murray et al.*, 2010], which is in contrast to the necessity of a crystallographic structure or insolubility requirement.

Mixed-phase clouds, which consist of supercooled droplets and ice crystals, exist between ~236 K and 273 K [*Murray et al.*, 2012]. Within the numerous studies on ice nucleation, the atmospheric importance of the four heterogeneous ice nucleation modes which can occur in mixed-phase clouds has not been well quantified. From lidar observations it has been found that supercooled droplets are present prior to the formation of ice crystals in mixed-phase clouds [e.g., *Ansmann et al.*, 2009; *Westbrook and Illingworth*, 2011]. Liquid water droplets are a prerequisite for ice formation, and imply deposition nucleation in mixed-phase clouds plays a minor role [*Murray et al.*, 2012]. Due to thermophoretic effects, which is the force exerted by a temperature gradient, contact freezing could be the favored nucleation process for evaporating droplets, but these droplets might even evaporate before freezing [*Phillips et al.*, 2007]. Therefore, it is suggested that immersion freezing is the most important freezing mechanism in mixed-phase clouds.

Investigation of ambient INPs is feasible with various methods: INP concentration measurements of aerosol particles collected on filters [e.g., *Bigg*, 1967; *Klein et al.*, 2010; *Conen et al.*, 2012; *Ardon-Dryer and Levin*, 2014] or in solutions [e.g., *Hader et al.*, 2014] have been conducted at various field sites. Recent studies of immersion freezing INP concentrations apply a droplet freezing array for which a number of aerosol particles are collected in a solution, on a filter or by taking samples of cloud, rain, or snow water [e.g., *Hader et al.*, 2014; *Stopelli et al.*, 2014; *Wright et al.*, 2014; *Conen et al.*, 2012, 2015; *Joly et al.*, 2014; *Mason et al.*, 2015a, 2016]. In these measurements, the abundance of ice active particles is investigated in suspensions, which contain multiple aerosol particles and with that multiple potential INPs. The measured freezing temperature belongs to the most active INP per sample volume. These methods can be used for ambient studies; however, they are not able to investigate the ice nucleation activity of single-immersed aerosol particles with a high temporal resolution.

To investigate the variability in INP concentration, continuous flow diffusion chambers (CFDCs) measure the ice nucleation activity for individual particles in real time. Originally, a cylindrical design is from the Colorado State University (CSU-CFDC) [*Rogers*, 1988]. Ambient aerosol is exposed in the chamber to a well-defined region between the inner and outer ice-coated chamber walls, which are the source for water vapor and held at different temperatures creating a temperature gradient and allowing control of the supersaturation conditions at a desired sample temperature. The concentration of INPs is obtained by counting the ice crystals downstream of the chamber. A parallel-plate design following the same experimental principle is the Zurich Ice Nucleation Chamber (ZINC) [*Stetzer et al.*, 2008] and its portable version PINC for field studies [*Chou et al.*, 2011], as well as the horizontal parallel-plate design by the University of Toronto (UT-CFDC) [*Kanji and Abbatt*, 2009]. Studies with CFDC instruments observe ice nucleation in the water subsaturated regime and a few percent in relative humidity (RH) above water saturation [e.g., *Rogers et al.*, 1998; *DeMott et al.*, 2010; *Chou et al.*, 2011; *Boose et al.*, 2016] but cannot isolate the immersion freezing mode with CCN activation prior to exposure to ice nucleation temperatures. To our knowledge, only four other instruments are able to activate single aerosol particles into cloud droplets prior to further supercooling at which ice nucleation is studied. These techniques are the Immersion Mode Cooling chAmber (IMCA) [*Lüönd et al.*, 2010; *Welti et al.*, 2012] coupled to ZINC and the Leipzig Aerosol Cloud Interaction Simulator (LACIS) [*Stratmann et al.*, 2004; *Niedermeier et al.*, 2010; *Hartmann et al.*, 2011]. Two other instruments utilizing the technique of cloud expansion chambers, the Aerosol Interaction and Dynamics in the Atmosphere (AIDA) cloud chamber [*Niemand et al.*, 2012] and Manchester Ice Cloud Chamber (MICC) [*Connolly et al.*, 2012] are able to investigate immersion freezing of single-immersed particles while achieving water drop activation at supercooled conditions prior to freezing.

CCN activation of aerosol is achieved at temperatures above the freezing point of water in IMCA, the vertical extension of ZINC. Cloud droplets with single-immersed aerosol particles are subsequently cooled prior to ice nucleation in ZINC. LACIS is a laminar flow tube with a total length of 7 m, where water vapor is sourced from humidified sheath air. The aerosol is exposed to supersaturation conditions by controlled cooling of prehumidified air. Additional cooling results in immersion freezing of supercooled cloud droplets at the ice nucleation temperature. By contrast, the AIDA cloud chamber and the MICC are not continuous flow diffusion but expansion chambers. Aerosol particles are dispersed into the chamber prior to an expansion experiment already at supercooled temperatures. The aerosol vessel is evacuated to reduce the pressure, which allows a controlled further decrease in temperature in the chamber and leads to supersaturation conditions resulting in the formation of a liquid cloud in which ice nucleation can occur. All four methods are laboratory instruments and are stationary.

In this work, we present the newly developed Portable Immersion Mode Cooling chAmber (PIMCA) instrument as an extension to PINC, allowing activation of aerosol particles to cloud droplets for immersion mode experiments on single-immersed aerosol particles. PIMCA is portable and can be deployed in the field and to other laboratories for measurement campaigns. We introduce the advanced design and discuss adaptations in comparison to the laboratory chamber IMCA [*Lüönd et al.*, 2010]. Validation experiments coupled to PINC [*Chou et al.*, 2011] are presented. Droplet evolution calculations and validation experiments support calculations of residence time, droplet size, and comparison to reference aerosols, respectively. Data obtained during the first field study with PIMCA-PINC conducted in spring 2014 at an urban-forest site in Switzerland are presented. The atmospheric implications of the experiments are discussed.

## 2. Experimental Method

The experimental method used for this study comprises of three main devices to measure immersion mode ice nucleation, namely, PINC (section 2.1), its vertical extension for immersion mode experiments, PIMCA (section 2.2) and for ice detection, the Ice Optical DEtector, IODE (section 2.3). A schematic of the instrumental setup is shown in Figure 1. In the immersion freezing mode conducted in this work, aerosol particles are first activated and grown to cloud droplets in PIMCA. Droplets containing one immersed particle are supercooled before freezing occurs at isothermal conditions in the main chamber of PINC at water saturation. Ice crystals and cloud droplets are detected at the bottom of the chamber with IODE to obtain a frozen fraction (FF).

### 2.1. PINC

PINC has previously been described in detail by *Chou et al.* [2011]. Briefly, it is a continuous flow diffusion chamber, and its measurement principle follows the CSU-CFDC [*Rogers*, 1988]. PINC can be operated for sampling in the temperature range 231–265 K. At the extreme ends of the temperature range, the instrument can be run from below water saturation to a maximum relative humidity with respect to water, $RH_w = 100\%$. For intermediate temperatures $RH_w$ up to 108% can be achieved depending on set sample $T$. The instrument is a vertical chamber consisting of two temperature controlled parallel walls. Prior to an experiment, a thin ice layer is generated on the inner chamber walls. To achieve supersaturation conditions with respect to ice, a (horizontal) temperature gradient is applied between the chamber walls. This results in a parabolic ice supersaturation profile between the two chamber walls with its peak saturation closer to the colder wall. The sample aerosol flow is layered within a particle-free sheath air flow on either side of the aerosol layer to ensure well-defined temperature and relative humidity conditions in the sample layer. The lowest section of PINC is an evaporation section, whose walls are both held at the same temperature as the warm wall of the PINC main chamber to maintain ice saturation but water subsaturation causing small droplets to evaporate. This feature is needed for deposition nucleation/condensation freezing experiments, for which an optical particle counter (OPC) distinguishes ice crystals from unactivated aerosol only by a size threshold. More details on PINC experiments on a variety of aerosol samples and field studies can be found elsewhere [*Chou et al.*, 2011; *Kanji et al.*, 2013; *Hiranuma et al.*, 2015; *Wex et al.*, 2015; *Boose et al.*, 2016].

### 2.2. Portable Immersion Mode Cooling chAmber (PIMCA)

The design of PIMCA follows the same parallel plate geometry as PINC but with a narrower plate distance in the upper droplet creating section for good control of $T$ and RH. Both walls are temperature controlled in order to apply a lateral temperature gradient between the plates. Additionally, a vertical temperature gradient along each wall is applied in order to gradually transition the droplets to the subzero temperatures in PINC. As a source of water vapor and to create supersaturation with respect to water in the chamber, continuously wetted filter papers are mounted to the inner walls of PIMCA (Figure 1, blue layer on PIMCA inner walls).
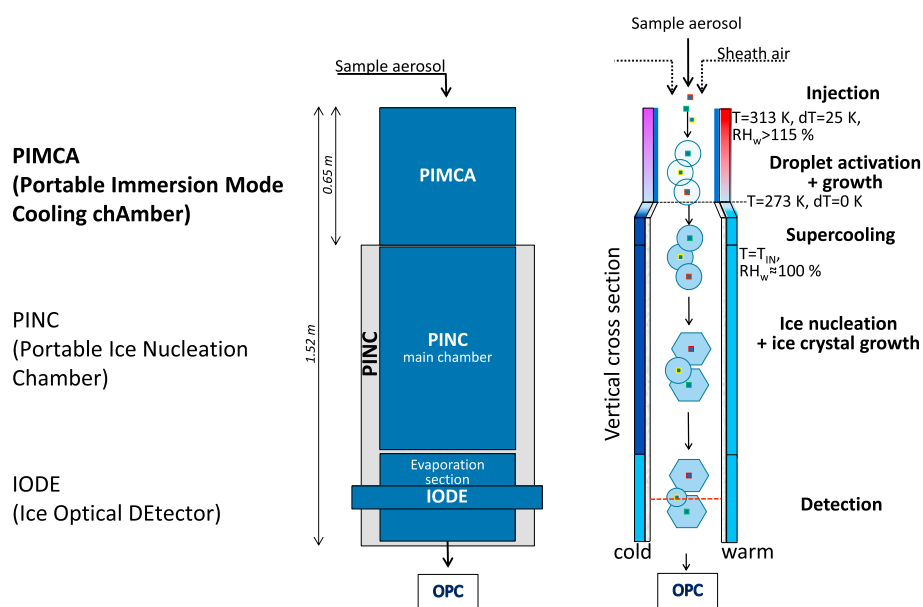
**Figure 1.** PIMCA-PINC instrumental setup. (left) The three main chamber sections and the two detection devices (IODE and the optical particle counter (OPC)—the latter is used for the PINC-mode only) in frontal view. (right) A vertical cross section of the chamber illustrates the particle trajectory during the experiment. IODE is positioned at the evaporation section, and the laser beam is indicated as orange line. A horizontal temperature gradient ("cold" and "warm") as well as a vertical temperature gradient is applied to the chamber walls. The color code represents the temperature of the chamber walls. PIMCA has a cold (purple) and warm (red) chamber wall at $T > 273$ K. In PINC, wall temperatures are cold (dark blue) and warm (blue) at $T < 273$ K. The evaporation section in PINC is held at the PINC warm wall temperature without applying a horizontal temperature gradient (blue). Inner chamber walls are lined with humidified filter paper in PIMCA (dark layer) and with an ice layer in the lower section of PIMCA and PINC (light grey layer).

The PIMCA-PINC setup has a total height of 2.1 m (net chamber size 1.52 m). In the upper part of the chamber, a wall temperature difference $\Delta T = 25$ K is controlled by heating and cooling units for a sample temperature of $T = 313$ K after the aerosol particles have entered the chamber through a vertical and preheated sample inlet ($T = 313$ K) into the droplet activation and growth section. In this section the wall distance is 5 mm, and flow rates are kept at 0.6 lpm for the sample air and 2.2 lpm for each of the particle-free sheath air flows, generating an aerosol layer with a width of less than 0.5 mm calculated based on the buoyancy flow profile in the chamber. The thermoelectric "zero line" cooling unit, which separates the warm and the cold section of PIMCA (273 K line) and the lower cooling unit are independently controlled by Peltier-cooling modules with air ventilation. The chamber below the zero line is a transition region where the droplets are supercooled and brought to a temperature closer to the experimental conditions in PINC with chamber walls covered with a thin ice layer (Figure 1, light grey layer in the lower section of PIMCA and on PINC inner walls). In this region, the plate distance is increased to 10 mm to adjust to the PINC dimensions. By increasing the chamber width, the flow velocity in the lower part of PIMCA and in PINC is reduced, which gives droplets more time to equilibrate to the colder temperatures before entering PINC. An advantage of keeping the flow rates in PINC at 0.6 lpm/4.4 lpm (sample/sheath) flow rate setting is a longer residence time of supercooled cloud droplets under ice nucleation conditions (cf. section 2.4).

### 2.3. Detection of Freezing

IODE is used to detect and distinguish between ice crystals and water droplets. The detector is placed at the evaporation section of PINC, 0.15 m below of the main chamber (Figure 1, orange line). This leads to partial evaporation of the droplets due to the subsaturated conditions with respect to water in the evaporation section of PINC (see section 2.4 for more details).

The ice nucleation activity of aerosol particles is obtained as a FF of droplets containing the aerosol as described in detail by *Nicolet et al.* [2010] and *Lüönd et al.* [2010]. Briefly, IODE uses linear polarized laser light, which is horizontally directed through the PINC chamber at the end of the ice growth section. To distinguish between ice crystals and water droplets, backscattered light intensity is detected in a parallel

and a perpendicular channel (angle of 3° of the horizontal plane). A wavelet peak detection algorithm is used to find the intensity peaks from individual particles in the backscattered signal, which allows single peak detection [*Lüönd et al.*, 2010]. The depolarization ratio $\delta$ is obtained from the signal intensities from the parallel and the perpendicular channel, according to *Nicolet et al.* [2010],

$$\delta = \frac{I_\perp}{I_\| + I_\perp},\tag{1}$$

with the signal intensities $I_\|$ and $I_\perp$ being the parallel and perpendicular channel, respectively. Ice crystals, which are aspherical return a higher depolarization signal (depolarization ratio) than the spherical cloud droplets. *Lüönd et al.* [2010] found that to a certain extent even small spherical water droplets return a perpendicular signal, making it impossible to distinguish their depolarization signal from the signal of ice crystals. To account for this effect, they experimentally determined a minimum depolarization threshold of $\tau_\delta = 0.07$ which is applied so that water droplets are not falsely detected as ice crystals. Based on experiments reported by *Nicolet et al.* [2010], unactivated aerosol particles generate a small signal, which is not detected as a peak in the analysis algorithm [*Lüönd et al.*, 2010]. For mineral dust aerosol, particles up to a size of about 800 nm remain undetected due to their low scattering signal [*Nicolet et al.*, 2010; *Lüönd et al.*, 2010].

Before each measurement, the background in the backscattered signal is determined using particle-free sample air. The background is subtracted from the signal. Main sources of the background are reflections from the chamber ice-coated walls or frost particles in the chamber. The input particle concentration is diluted to $20–100\ cm^{-3}$, which allows for distinguishable single-intensity peaks and prevents coincidence of multiple particles in the laser beam. The FF is given by the ratio of ice crystals to the total particle number detected by IODE:

$$FF = \frac{N_\text{ice}}{N_\text{ice} + N_\text{droplets}},\tag{2}$$

where $N_\text{ice}$ is the number of ice crystals and $N_\text{droplets}$ is the number of water droplets detected per experiment. The error in FF is based on measurement uncertainties of the detector, which arise due to electronic noise in the signal intensities of $I_\|$ and $I_\perp$. Error propagation on equation (1) leads to the error in the depolarization ratio $\Delta\delta$ as reported in *Lüönd et al.* [2010]:

$$\Delta\delta = \frac{1}{(I_\| + I_\perp)^2} \sqrt{I_\|^2(\Delta I_\perp)^2 + I_\perp^2(\Delta I_\|)^2}\tag{3}$$

for which the standard deviations of the mean background in the parallel and perpendicular channels are used for the measurement errors $\Delta I_\|$ and $\Delta I_\perp$ of the signal intensities in both channels. For experiments with depolarization ratios close to the threshold $\tau_\delta$, a misclassification of the particle is possible. Thus, a particle with $\delta > \tau_\delta$ and $\delta - \Delta\delta < \tau_\delta$ is classified as an ice crystal but could be a potentially miscounted ice peak. The ratio of such peaks and the total particle number is indicated as the lower error bar and vice versa for potentially misclassified water droplets as the upper error bar. For better counting statistics, each data point shown in the plots hereafter is based on two to five individual measurements, each of at least 1000 individual (particle) intensity peaks detected at the same $T$. In addition to the measurement uncertainty from IODE, the statistical uncertainty is added. The statistical error $\Delta FF_\text{stat}$ is obtained as

$$\Delta FF_\text{stat} = \frac{FF_\text{max} - FF_\text{min}}{2\sqrt{N}}\tag{4}$$

where $FF_\text{max}$ and $FF_\text{min}$ are the maximum and minimum values from the averaged data and $N$ the number of measurements per temperature averaged. FF values presented in the following are shown as averaged data per temperature.

## 2.4. Simulation for Droplet Evolution in PIMCA-PINC

To ensure that cloud droplets in PIMCA grow to sizes large enough to reach the detector, computational fluid dynamics (CFD) simulations with FLUENT 14.0 [*ANSYS*, 2011] were conducted. The simulations were setup in a vertical cross section taking into account chamber wall humidification and ice layers. A 2-D simulation is considered valid, because particles are only injected over a width of 0.27 m into the chamber with a 15 mm particle-free region on either side adding up to a total width of 0.3 m (Figure 1, left, frontal view). This means
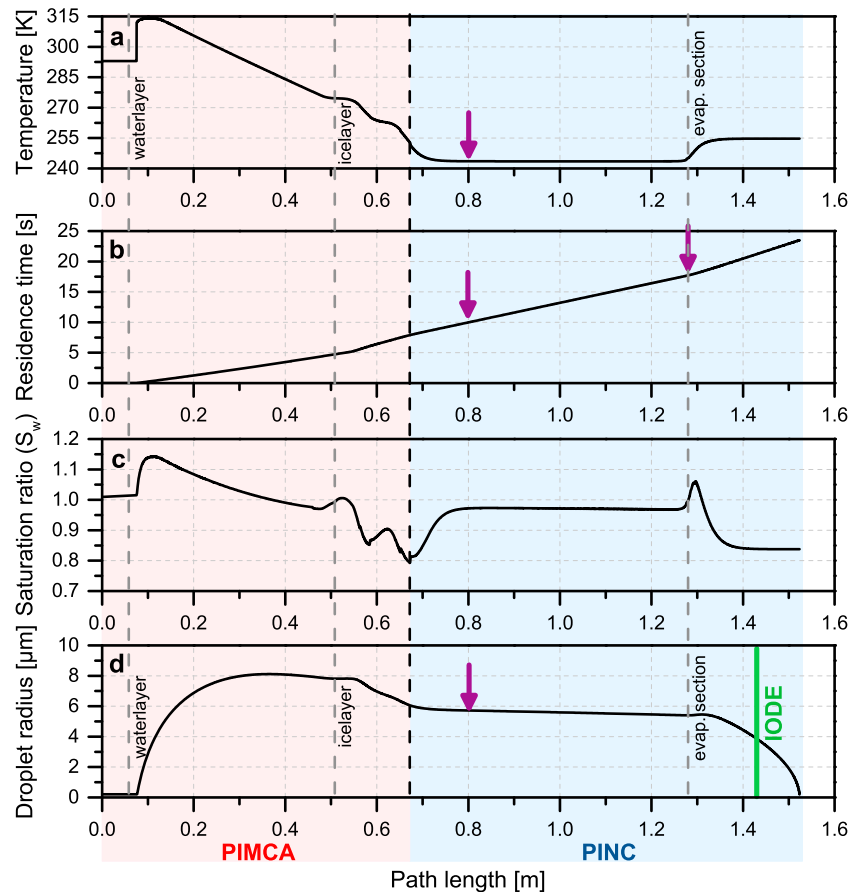
**Figure 2.** Simulation of the droplet evolution in PIMCA-PINC. The calculations are based on $T = 243$ K in PINC. Sample layer conditions were obtained based on simulated particle trajectories [*ANSYS*, 2011] to calculate diffusional growth and evaporation of cloud droplets in the setup along the path length of the PIMCA-PINC setup, given as (a) the temperature, $T$; (b) the residence time, $t_{res}$; (c) the saturation ratio, $S_w = RH_w/100\%$; and (d) the droplet radius, $r$. The detection device IODE (green vertical line) is positioned 1.43 m after the sample air inlet. Purple arrows indicate the position where the experimental conditions for ice nucleation conditions are reached.

**Table 1.** Properties and Experimental Parameters Under Typical Operation Conditions of the PIMCA-PINC Setup Compared to the Laboratory Version IMCA-ZINC[a]

|  | PIMCA(-PINC) | IMCA(-ZINC) |
|---|---|---|
| Application | Field and lab | Lab only |
| Flow rate sample | 0.6 lpm | 1 lpm |
| Flow rate total | 5 lpm | 5 lpm (10 lpm in ZINC) |
| Droplet size $r$ | 5–7 µm | 10 µm [*Welti et al.*, 2012] |
| Residence time $t_{res}$ | 7 s | 10 s [*Welti et al.*, 2012] |
| Length immersion chamber | 0.65 m | 0.72 m |
| Dimensions setup (net chamber) | 2.1 m (1.52 m) | 2.8 m (2.47 m) |
| Cooling system | Peltier elements (compressors) | Ethanol cooling system |
| Sheath air humidification | No | Yes |

[a]Droplet size and residence time refer to periods of ice nucleation conditions in the experiment.
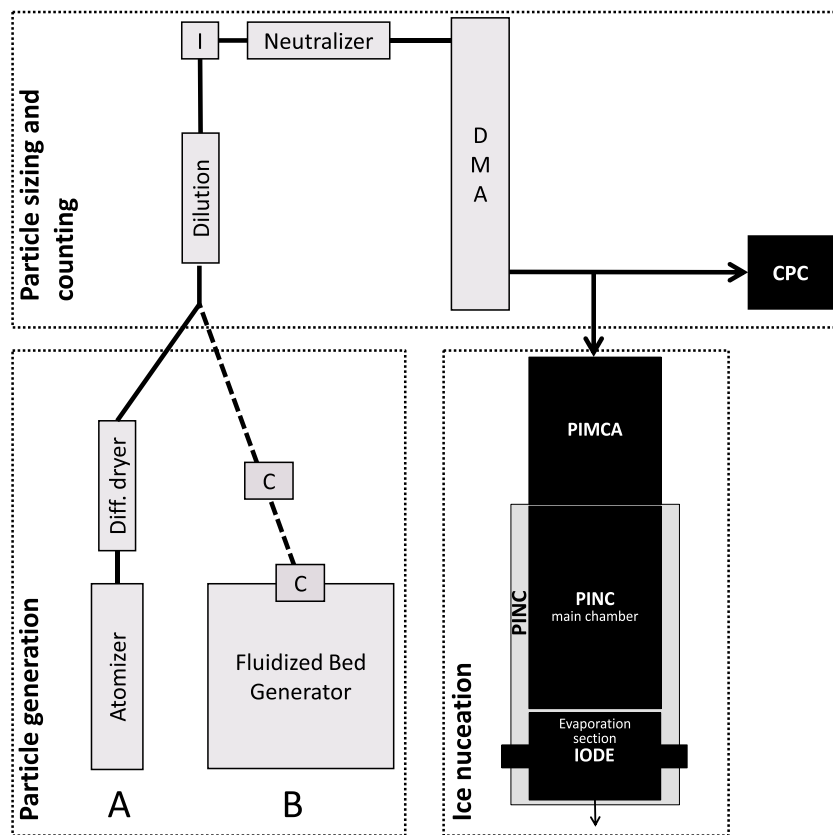
**Figure 3.** Instrumental setup for experiments during validation tests in the laboratory for particles generated from an aqueous solution (A) or dry dispersed particles (B). Depending on the setup used, two cyclones (C) and an impactor (I) were used prior to size selection with a Differential Mobility Analyzer (DMA). The aerosol particle concentration (after the dilution stage) was measured with a Condensation Particle Counter (CPC).

that the interaction of the sample flow with the side walls of the chamber can be neglected (see *Lüönd et al.* [2010] for similar simulations for IMCA). Temperature input parameters for the CFD simulation of the chamber were obtained experimentally along the PIMCA-PINC setup. The trajectories of spherical cloud droplets with the radius of 6 μm are derived from the CFD simulation. Diffusional growth and evaporation of droplets are calculated along the trajectory based on the simulated conditions in the sample lamina (temperature, saturation ratio with respect to water, and velocity) starting with a droplet size of $d = 400$ nm once water saturation is reached (0.075 m downstream of the aerosol inlet). In Figure 2 the conditions are shown along the droplet path after entering the PIMCA-PINC setup including diffusional growth and evaporation. The dry sample aerosol and particle-free sheath air enter the chamber at $T = 303$ K. After 0.05 m, heating units on each wall increase the temperature in the sample layer to a droplet activation temperature ($T = 313$ K) reaching water saturation conditions after 0.025 m along the particle trajectory. Activated particles nucleate and grow to cloud droplets with $r = 8$ μm after exposure to the maximum $RH_w > 115\%$ in the chamber. Humidified inner walls in the warm section of PIMCA are indicated as "water layer" by a dashed line in Figure 2. Cloud droplets are subsequently cooled down before entering the subzero temperature region of PIMCA. At the "zero line" position, both chamber walls are set to identical temperatures. Below this section, the plate distance is widened from 5 mm to 10 mm to adjust to the chamber dimensions of PINC. An additional Peltier-based cooling unit in the lower part of PIMCA provides further supercooling and supersaturation with respect to ice prior to encountering conditions in PINC. In PINC the droplet with an immersed aerosol particle is exposed to the experimental conditions for ice nucleation (for this CFD example, $T = 243$ K at water saturation) for ~7 s (indicated by purple arrows) before entering the evaporation section. On average, a droplet reaching ice nucleation conditions is simulated to grow to a droplet radius between 5 μm and 7 μm depending on $T$ in PINC. According to the calculated evaporation processes in the lower section of PINC, droplets reach a radius of $r \approx 4$ μm at the position of IODE (path length $= 1.43$ m) and confirms the detectability of droplets at the position of the detector (see section 2.3). This theoretically confirmed the feasibility of the new design.
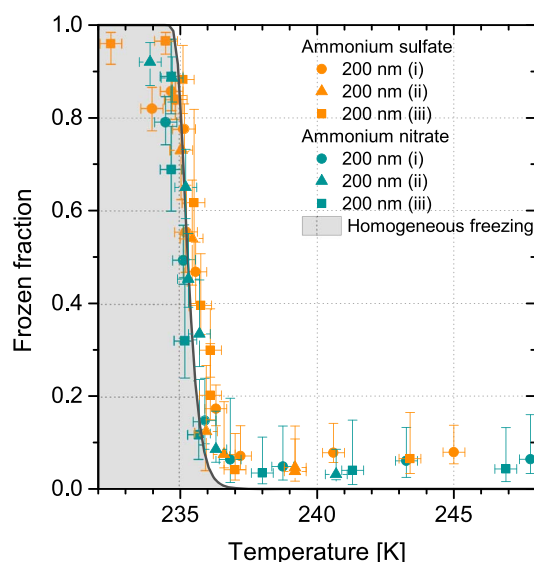
**Figure 4.** Results of homogeneous freezing experiments on size-selected ammonium sulfate and ammonium nitrate particles each from three independent experiments (i–iii). Shaded area: The temperature regime which is dominated by homogeneous freezing of droplets with radius $r = 6$ μm and $t_{res} = 7$ s calculated with homogeneous nucleation rates reported by *Earle et al.* [2010].

### 2.5. The PIMCA-PINC Specifications

Although the experimental principle is unchanged from the IMCA-ZINC laboratory version [cf. *Lüönd et al.*, 2010], a major redesign was necessary to adapt to portable dimensions. The differences of the portable PIMCA-PINC setup to the laboratory version are summarized in Table 1.

An advantage of PIMCA is the Peltier-controlled cooling system, which allows the temperature control independently from PINC and does not require cooling liquid nor compressors. PIMCA-PINC can be operated in the immersion mode from 233 K to 263 K ensuring at least $RH_w = 100\%$ in PINC to prevent evaporation of cloud droplets. The given temperature range is limited by the cooling power of PIMCA-PINC and by the temperature of the warm wall in PINC to ensure that the ice layer on the chamber wall does not melt. The shorter chamber dimension of PIMCA-PINC (1.52 m net chamber size) allows easy transport and shipping and allows the possibility for deployment in remote measurement stations, e.g., in a measurement trailer or participation in lab campaigns internationally. The flow rates are set to lower flows to allow enough time for particles to grow to detectable cloud droplet sizes. In recent studies, IMCA-ZINC has been used at a total flow rate of 10 lpm by adding additional sheath air in the transition zone between IMCA and ZINC [*Welti et al.*, 2012] or without additional sheath air at 5 lpm [*Lüönd et al.*, 2010]. Because PINC is shorter than ZINC, it has a residence time of only 4–5 s at 10 lpm total flow. When operated with PIMCA, a total flow rate of 5 lpm is used in the PIMCA-PINC setup. This increases the available ice nucleation time to ∼7 s and thereby reduces the residence time effects on the measured FF. Cloud droplet sizes reach $r = 5–7$ μm and are smaller compared to $r = 10$ μm in ZINC. The reason is the different water-subsaturated transition zones between droplet activation and ice nucleation conditions in the lab and in the portable chamber where droplets shrink. Based on the limitations of the cooling power in the lower section of PIMCA in transitioning to $T$ in PINC, more evaporation results in smaller droplet sizes entering PINC in comparison to IMCA-ZINC. In addition to the humidification of the chamber walls, in IMCA the sheath air is humidified via nafion humidifiers. This was not done in the portable setup after obtaining an insignificant decrease in droplet size (from droplet evolution simulations) without additional humidification of the sheath air. To improve the particle transmission efficiency, the horizontal aerosol inlet is replaced by a vertical version.

## 3. Instrument Validation Experiments

### 3.1. Setup for Laboratory Studies

Validation and test experiments of the PIMCA-PINC setup were conducted under controlled laboratory conditions to calibrate RH and $T$ as well as cloud droplet size. Particles were generated either by atomization of an aqueous solution or dry dispersion (Figure 3). Aqueous solutions were aerosolized with a home-built atomizer for experiments with ammonium sulfate ($(NH_4)_2SO_4$) and ammonium nitrate ($NH_4NO_3$) dissolved in Milli-Q water (18.2 MΩ cm purity) in a 1 wt % solution. Solution droplets produced by the atomizer are dried in a series of two 1 m diffusion dryers and passed through an impactor to narrow the size distribution prior to size selection with a Differential Mobility Analyzer (DMA, Electrostatic Classifier, TSI Model 3081), which selects particle diameters based on electrostatic mobility. A Condensation Particle Counter (CPC, TSI Model 3772) measured the particle concentration entering the PIMCA-PINC setup. A dilution stage was used in the sample line to adjust the particle concentration in the sample flow. Dilution was necessary to avoid coincidence
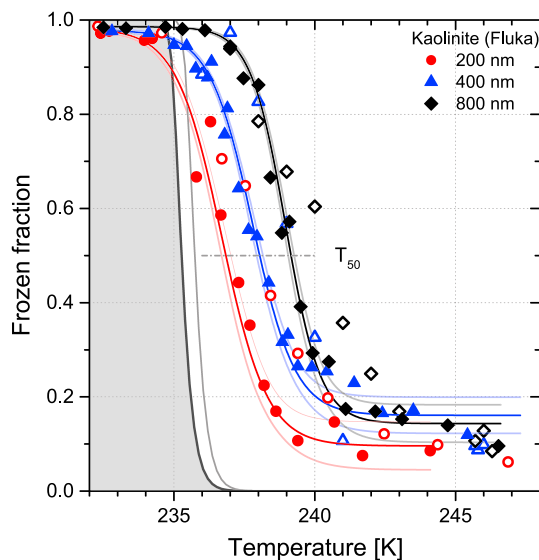
**Figure 5.** Validation experiments for heterogeneous freezing on kaolinite particles. Data from PIMCA-PINC (filled symbols) are shown in comparison to IMCA-ZINC data (open symbols; 400 nm and 800 nm data for $T < 245$ K from *Welti et al.* [2012]) for three different particle sizes. The homogeneous freezing regime is shaded in grey (for IMCA-ZINC as light grey curve; both calculated with homogeneous nucleation rates by *Earle et al.* [2010]). The median freezing temperature is indicated as the dash-dotted horizontal curve. Fit curves on the PIMCA-PINC data (including 95% confidence intervals) are shown as solid colored curves.

errors while ensuring appropriate counting statistics. For dry particle aerosolization of mineral dust particles (Kaolinite Fluka, Sigma-Aldrich), the sample material was dispersed with a Fluidized Bed Generator (FBG, TSI Model 3400A). Two cyclones ($D_{50} = 3$ μm (integrated in FBG) and an additional one ($D_{50} = 1$ μm)) were used upstream of the DMA.

### 3.2. Homogeneous and Heterogeneous Freezing on Well-Defined Aerosol Samples

Homogeneous freezing experiments were performed to characterize the instrument. Ammonium sulfate and ammonium nitrate were used as seed particles for cloud droplet formation to study the freezing of supercooled dilute aqueous droplets. Figure 4 summarizes the experimental results (FF as a function of $T$), where each aerosol type was evaluated in three independent measurements (i–iii) using 200 nm size-selected aerosol particles. Data are binned per temperature and experiment and compared to the theoretical predicted freezing curve for homogeneous freezing of $r = 6$ μm droplets and a residence time of $t_{res} = 7$ s (cf. section 2.4) shown as a black line in Figure 4. The theoretical line is based on the homogeneous nucleation rate reported by *Earle et al.* [2010] taking into account $t_{res}$ and droplet volume. The experimental data coincide with theory and have a good reproduci-

bility between three independent experiments. A heterogeneous freezing signal was not expected for these experiments and was not observed. Small FF for heterogeneous freezing temperatures ($T > 236$ K) are in the background (low signal-to-noise ratio) of the detector of FF $\approx 0.1$.

For comparison with the laboratory setup, IMCA-ZINC, the experiments were conducted with kaolinite. Particles were dry dispersed and size-selected at 200 nm, 400 nm, and 800 nm for comparison. Figure 5 shows an overview of PIMCA-PINC (filled symbols) with two independent measurements per particle size including best fit curves with 95% confidence intervals and the IMCA-ZINC literature data (open symbols; 400 nm and 800 nm data for $T < 245$ K from *Welti et al.* [2012]). The grey area represents the temperature regime where homogeneous freezing is expected [*Earle et al.*, 2010]. This region extends to about 0.5 K warmer temperatures for IMCA-ZINC measurements due to longer residence time and larger droplet sizes (see Table 1). The homogeneous freezing regime in IMCA-ZINC experiments is indicated by the light grey line in Figure 5.

The PIMCA-PINC data show a heterogeneous freezing signal with a clear size dependence showing a higher freezing efficiency for larger kaolinite particles. This is in agreement with previous results in which a comparable setup for particle generation was used [*Lüönd et al.*, 2010; *Welti et al.*, 2012]. The median freezing temperatures $T_{50}$, where 50% of the droplets are frozen, is found to be 236.8 K for the 200 nm particles and 238.0 K and 239.2 K for the 400 nm and 800 nm particles, respectively. Error bars are not shown for clarity (cf. Figure 6). $T_{50}$ from *Lüönd et al.* [2010] and *Welti et al.* [2012] from the laboratory version IMCA-ZINC at the same sample conditions are about 1 K higher. This discrepancy can arise, e.g., from the longer residence time in IMCA-ZINC. In Figure 6, exemplary time dependence during ice nucleation conditions are compared for 400 nm particles using data from *Welti et al.* [2012]. Shorter droplet residence time of $t_{res} = 6$ s (purple) instead of $t_{res} = 10$ s (orange) reduced FFs in *Welti et al.* [2012] to values within the uncertainty of PIMCA-PINC data obtained with $t_{res} = 7$ s. The lower limit in FF at warmer temperatures is slightly higher in PIMCA-PINC compared to *Welti et al.* [2012]. A possible reason is a smaller droplet size resulting in a lower signal-to-noise ratio.
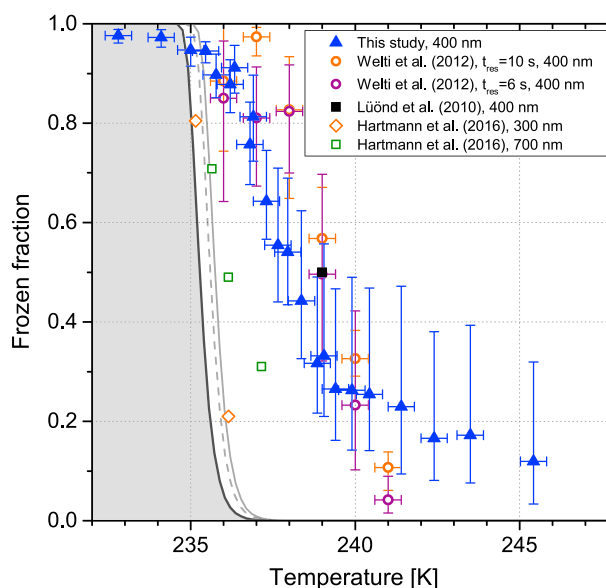
**Figure 6.** Heterogeneous freezing of size-selected kaolinite particles with PIMCA-PINC from this study (blue triangles) with $t_{res}$ = 7 s. Data from *Welti et al.* [2012] for the same sample as orange circles ($t_{res}$ = 10 s) and purple circles ($t_{res}$ = 6 s). Also shown are data from *Hartmann et al.* [2016] ($t_{res}$ = 1.6 s; without multiple charge correction) and *Lüönd et al.* [2010] ($t_{res}$ = 14 s). The shaded area is calculated based on the homogeneous nucleation rate reported by *Earle et al.* [2010] for PIMCA-PINC. The grey lines represent the homogeneous freezing regime for *Welti et al.* [2012] with $t_{res}$ = 10 s (solid) and $t_{res}$ = 6 s (dashed), respectively.

Data from immersion freezing techniques on single-immersed aerosol particles with the same kaolinite sample (Fluka, Sigma-Aldrich) are reported by *Augustin-Bauditz et al.* [2014], *Wex et al.* [2014], and *Hartmann et al.* [2016]. *Wex et al.* [2014] and *Augustin-Bauditz et al.* [2014] did not observe a $T_{50}$ for particles of 700 nm or smaller for their reported $T$ > 237 K. We compare to particle sizes which are closest to the size measured in this study. *Hartmann et al.* [2016] report $T_{50}$ between 235.5 and 236 K for particle sizes of 300 nm to 700 nm as shown by a selection of their data in Figure 6. The $T_{50}$ is 2–2.5 K lower compared to measurements from this study. The $t_{res}$ reported by *Hartmann et al.* [2016] is 1.6 s. The difference in observed $T_{50}$ between *Hartmann et al.* [2016] and the data from the current measurements could arise from the difference in residence time. The residence time of FF for this particular kaolinite sample has been shown by *Welti et al.* [2012]. A short residence time can lead to a lower FF and therefore lower $T_{50}$. Another reason could be that effective particle sizes could be larger in our study compared to those reported in *Hartmann et al.* [2016] due to multiply charged particles passing through the aerosol generation and size selection system.

## 4. Ambient In Situ Immersion Freezing With the PIMCA-PINC Setup During the ZAMBIS 2014 Field Study

### 4.1. Description of the Field Site and Instrumentation

In spring 2014 the Zurich AMBient Immersion freezing Study (ZAMBIS) was conducted to investigate the immersion freezing efficiency of urban aerosol particles during pollen season. The study was undertaken at an urban-forest site over a period of 6 weeks. The measurement site (47.406°N, 8.512°E, 540 m above sea level) was located in the northwestern periphery of the city of Zurich, Switzerland at an elevated area near the ETH Hönggerberg Campus. In situ ice nucleation measurements were conducted with PIMCA-PINC from within a mobile trailer on site. A schematic of the setup is shown in Figure 7. Aerosol inlet 1 was used for sampling aerosol for immersion freezing experiments. Bends in the sampling line allow mainly particles in the submicron size range to reach PIMCA-PINC (cf. Appendix C for characterization of particle losses). In addition, for experiments with PIMCA-PINC a dilution stage was used in the ambient sample line to avoid coincidence errors while ensuring appropriate counting statistics for particle detection with IODE. As shown in Figure 7, aerosol number concentrations after the dilution stage were measured with a CPC in parallel to measurements with PIMCA-PINC, similar to laboratory experiments. Measurements were taken as temperature scans approximately once to twice per day each with a sampling time of 1.5 − 2 hours. On the second total aerosol
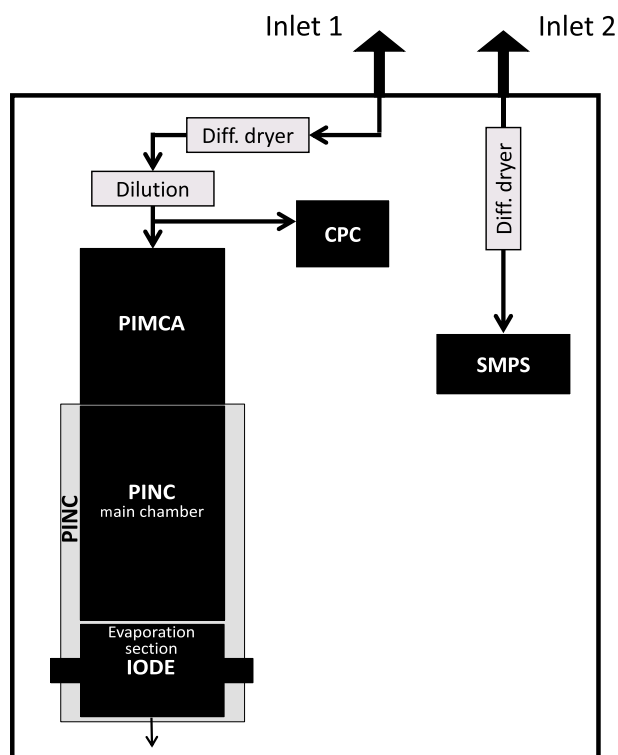
**Figure 7.** Experimental setup for ambient measurements during ZAMBIS. Inlet 1 was used for in situ immersion measurements with PIMCA-PINC. A dryer and a dilution stage were installed upstream of PIMCA-PINC. Aerosol particle number concentration was measured after dilution (CPC) parallel to the immersion freezing experiments. Inlet 2 was used for measurements of the aerosol size distribution (SMPS).

inlet 2, the aerosol size distribution was measured with a Scanning Mobility Particle Sizer (SMPS, custom built) [*Wiedensohler et al.*, 2012] for a size range from 10 nm to 880 nm. Additionally, meteorological conditions were monitored at the institute's weather station on site. Complimentary bioparticle detection, daily filters for particulate matter <10 µm ($PM_{10}$), and liquid impaction for drop freezing assay experiments were also collected. In this work we present and discuss the results from PIMCA-PINC.

### 4.2. Investigating the Frozen Fraction of Ambient Aerosol Particles

In situ ice nucleation experiments with PIMCA-PINC are analyzed to obtain the frozen fraction of activated particles. Temperature scans were started at homogeneous freezing temperatures with the first sample taken at $T < 234$ K and ended at warmer temperatures when FF did not show a further decrease with increasing temperature. Figure 8a summarizes the data throughout the period of the campaign with the date shown as one color per week. Each data point represents an average value of two to five measurements taken within a 5 min period at the same $T$, representing an average of $3600\pm1500$ individual (particle) intensity peaks analyzed per temperature. The temperature regime, which is dominated by homogeneous freezing, is indicated by the dark grey curve. Most data points are close to temperatures dominated by homogeneous freezing within a temperature uncertainty of $dT = 0.4$ K. The uncertainty in FF at warmer temperatures ($T > 236$ K) is increased due to smaller droplet sizes in ambient measurements. In field studies on polydisperse aerosol which can vary in composition and hygroscopicity, particles are activated to cloud droplets from the whole size distribution, which results in a wider distribution of droplet sizes compared to experiments on chemically similar and pure monodisperse aerosol. Therefore, the composition dependent hygroscopicity of the ambient aerosol can influence the droplet activation, growth, and the resulting droplet sizes. This effect leads to a higher uncertainty in the signal peak detection and therefore to a higher uncertainty in FF. To rule out possible miscounting (underestimation of droplets) due to small droplet sizes, which are not detectable by IODE, the total activation ($act_{tot}$) is obtained. The $act_{tot}$ is the ratio of the particle number detected by IODE ($N_{tot}$)
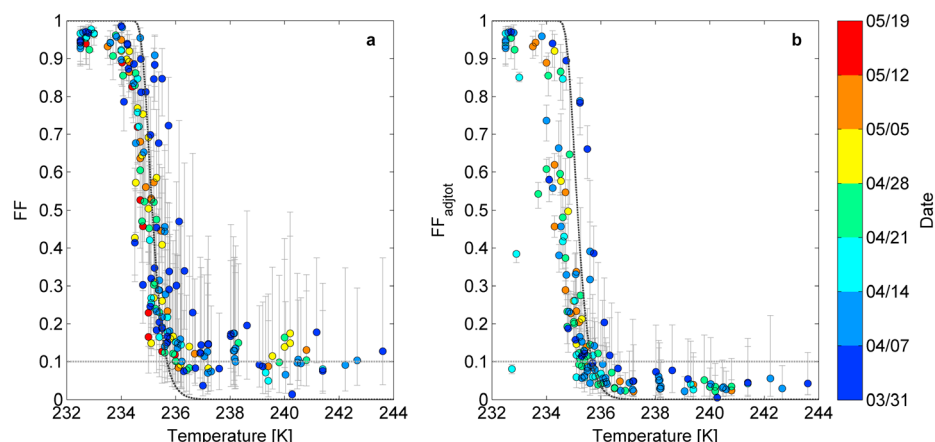
**Figure 8.** (a) The measured frozen fraction (FF) as a function of temperature for each experiment during ZAMBIS 2014. Data have been averaged for all data points (2–5) at each measured temperature. The dark grey line represents the homogeneous freezing regime. The horizontal dashed line shows the detection limit. (b) Data from Figure 8a after adjustments considering undetected droplets in IODE as reported in section 4.2.

per interval (35 s) and the sampled aerosol particle number per sample interval after the dilution stage ($N_{CPC}$), which is measured upstream of PIMCA-PINC with a CPC. The $act_{tot}$ is then given by

$$act_{tot} = \frac{N_{tot}}{N_{CPC}} \qquad (5)$$

and presented as a function of $T$ in Figure 9a. A temperature dependent decrease of $act_{tot}$ is observed. This indicates that activated particles did not grow large enough or that the droplets partly evaporated and remained at an undetectable size at warmer temperatures. During the experiment, the dilution of the ambient aerosol was reduced (thus increasing the sampled aerosol number) at higher temperatures to counteract the decrease in the detected particle number in IODE. The particle concentrations were measured after the dilution stage upstream of PIMCA-PINC and are shown in Figure 9d. A decrease in the number of detected particles with increasing temperature is not observed for experiments with size-selected particles in the laboratory (a comparison for polydisperse and monodisperse experiments can be found in Appendix B). As can be expected, the detected liquid fraction increased with temperature (Figure 9b) while the detected ice fraction decreased with increasing $T$ (Figure 9c). To consider undetected cloud droplets and therefore the potential to overestimate FF, the following adjustment is introduced, where $N_{tot}$ is adjusted based on $N_{CPC}$.

In the homogeneous freezing temperature regime, all droplets freeze and grow to large ice crystals which can be detected reliably. Therefore, at the coldest measured temperature, the highest number of frozen CCN activated particles will be counted by IODE. With this assumption, the maximum detected activation for each temperature scan is reached at the coldest temperature ($T_0$) measured at $T_0 < 234$ K and with that at $act_{tot}(T_0)$. Accordingly, the maximum possible counts detectable by IODE are:

$$\text{max counts} = act_{tot}(T_0) \cdot N_{CPC} \qquad (6)$$

which leads to an adjusted frozen fraction $FF_{adjtot}$ including undetectable particles by IODE in the form:

$$FF_{adjtot} = \frac{N_{ice}}{N_{ice} + N_{droplets} + N_{nd}} = \frac{N_{ice}}{\text{max counts}} = \frac{N_{ice}}{N_{CPC}} \frac{N_{CPC}(T_0)}{N_{tot}(T_0)} \qquad (7)$$

with $N_{nd}$ being the undetected number of aerosol particles based on the maximum fraction at the beginning of each experiment. The ratio of undetectable particles to the total sampled particle number per interval (Figure 9e) is given by

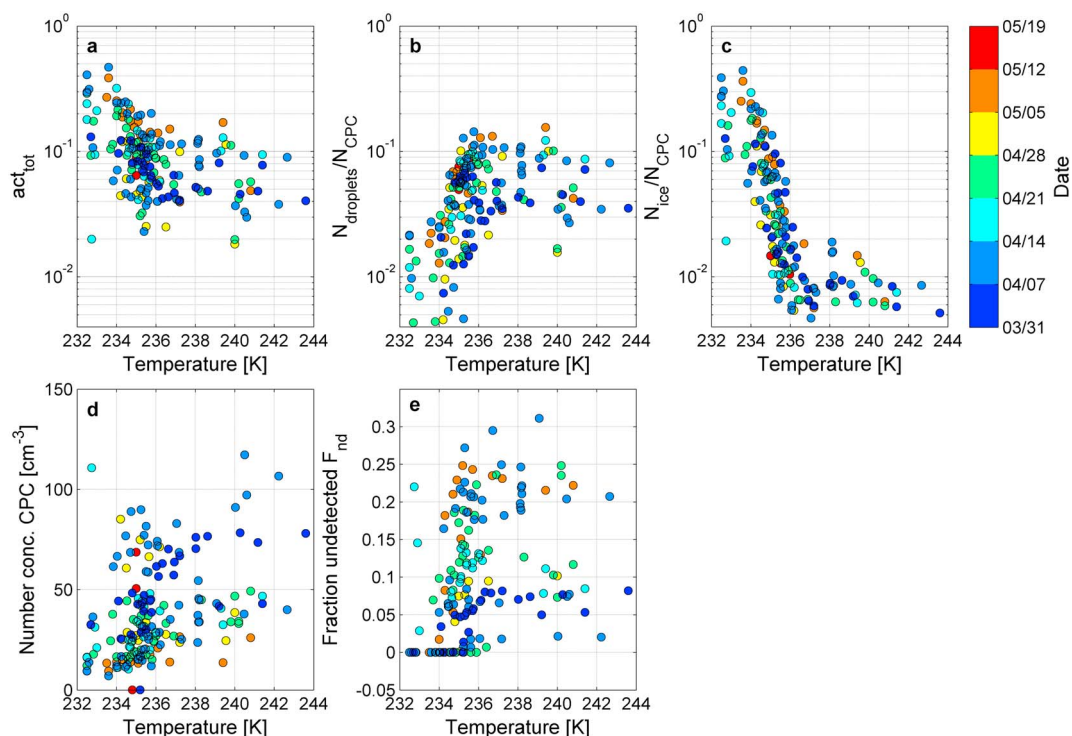$$F_{nd} = \frac{N_{nd}}{N_{CPC}}. \qquad (8)$$

**Figure 9.** Activation of ambient aerosol in PIMCA-PINC. Detected aerosol particles are distinguished into (a) total activated particles, (b) droplets, and (c) ice crystals detected by IODE as a fraction to the entering aerosol. (d) Sampled interstitial aerosol concentration was measured with a CPC after the dilution stage for the ambient sample parallel to the PIMCA inlet. (e) The fraction of undetected particles by IODE is given.

Depending on the experiment and measured temperature, the fraction of undetected particles $F_{nd}$ can range up to 30% of $N_{tot}$ and increases with increasing temperature. This indicates that a substantial fraction of cloud droplets are too small to remain at a detectable size at the position of the detector. Major differences are found between experimental days which can arise from differences in the ambient particle size distribution and composition, where the latter may influence the hygroscopicity and therefore the ability to grow. This could be the case for, e.g., freshly emitted soot from traffic or wood fires.

The adjusted frozen fraction $FF_{adjtot}$ is given in Figure 8b. Compared to the raw data (Figure 8a), the $FF_{adjtot}$ lie close to the temperatures which are dominated by homogeneous freezing. Some exceptions are found in the week of 14 April 2014 to 21 April 2014. The number concentration measured with the CPC (Figure 9d, cyan)



**Figure 10.** Measured ambient size distribution during PIMCA-PINC measurement periods.

during this period was higher at $T < 234$ K. Changes in the particle concentration during the period could be due to local influences. Overall, $FF_{adjtot}$ for $T > 236$ K are found to be low, which supports the assumption of ice overestimation before the adjustment. The measurement uncertainty is lowered by applying this adjustment. $FF_{adjtot}$ larger than 0.1 are reliable measurements within the instruments uncertainties and is the typical lower limit found for laboratory studies (see section 3.2). Day-to-day variations in the freezing curves are within the uncertainty of $dT = \pm 0.4$ K of the experiment. However, data taken at the beginning of April (before 7 April 2014, dark blue) indicate a more ice nucleation active aerosol. Parallel size distribution measurements (Figure 10) show a higher concentration of particles with a diameter larger than 100 nm,
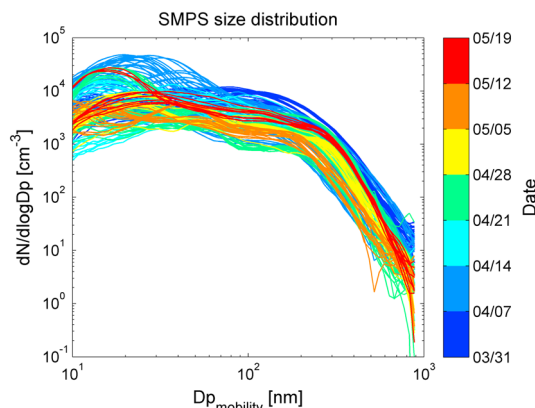
**Table 2.** CCN Concentrations for ZAMBIS Aerosol Particle Concentrations Measured From 10 nm to 880 nm for Typical Ambient Supersaturations SS Based on the CCN Activated Fraction $A_{CCN}$ from *Paramonov et al.* [2015], *Andreae* [2009], and *Madonna* [2009]

| | SS | Mean $N_{CCN}$ | Minimum to Maximum $N_{CCN}$ | |
| --- | --- | --- | --- | --- |
| | (%) | (cm$^{-3}$) | (cm$^{-3}$) | $A_{CCN}$ |
| Global average [*Paramonov et al.*, 2015] | 0.3 | 3450 | 916–11040 | 0.43 ± 0.12 |
| Polluted continental conditions [*Andreae*, 2009] | 0.4 | 2992 | 776–9352 | 0.36 ± 0.12 |
| Urban/ZH [*Madonna*, 2009] | 0.3 | 1461 | 388–4676 | 0.18 ± 0.09 |

possibly from a local source. Larger aerosol particles are typically more efficient INP and therefore are expected to contribute to a higher FF$_{adjtot}$ compared to smaller aerosol particles. Even though no distinct heterogeneous freezing signal could be detected for the majority of the data points within the instrumental uncertainty, it is likely that bursts of particles are found to be active immersion freezing nuclei. Concentration of ambient particles triggering heterogeneous nucleation are expected to be some orders of magnitudes smaller than CCN active particles (only 1 in 10$^6$ of the total aerosol particles at $T = 253$ K) [*Seinfeld and Pandis*, 2006] and therefore below the detection limit of the measurement method with IODE for $T > 236$ K.

### 4.3. Atmospheric Implication of Observed Ice Nucleation With PIMCA-PINC

Experiments in PIMCA are obtained at RH$_w$ > 115% in order to activate each aerosol particle to a cloud droplet. In the atmosphere, typical supersaturations for CCN activation in the polluted boundary layer are found to usually remain below 0.3%, but can reach 1.0% in clean and convective conditions [*Ditas et al.*, 2012; *Hammer et al.*, 2014; *Hudson and Noble*, 2013]. Therefore, it has to be taken into account that under atmospheric conditions not all aerosol particles activate to cloud droplets, like in PIMCA due to the higher supersaturation. Immersion freezing in the atmosphere depends on the number of cloud droplets available. The number of particles activating into cloud droplets during ZAMBIS is estimated using typical atmospheric supersaturations (0.3–0.4%). The CCN concentration during ZAMBIS was not measured on site (e.g., with a CCN counter) and is therefore estimated as follows.

The CCN activated fraction ($A_{CCN}$) is defined as the fraction of ambient aerosol acting as CCN and therefore represents the activation of cloud droplets under the given supersaturation conditions. *Paramonov et al.* [2015] proposed a function, representing the average CCN activated fraction from ambient aerosol, $A_{CCN,global}$ for eight field sites around the world as a function of supersaturation SS [%] given as

$$A_{CCN, global} = 0.22 \cdot \ln(SS) + 0.69. \qquad (9)$$

Assuming a typical atmospheric supersaturation SS = 0.3% in the boundary layer, the CCN activated fraction is $A_{CCN, global} = 0.43 \pm 0.12$. However, a global average for CCN activation may be incorrect for the local properties at the urban forest site. *Andreae* [2009] summarized various studies on polluted continental CCN properties and obtained an average $A_{CCN,poll} = 0.36 \pm 0.12$ at a supersaturation of SS = 0.4%. In a third study, *Madonna* [2009] reported CCN measurements at a polluted urban location in the city of Zurich and found for SS = 0.3% $A_{CCN,ZH} = 0.18 \pm 0.09$ corresponding to CCN concentrations of ~1700 cm$^{-3}$ for measurements during their study in Zurich. For the three cases, the CCN concentration $N_{CCN}$ during ZAMBIS with the total ambient aerosol concentration, $N_{amb}$, between 10 nm and 880 nm is calculated:

$$N_{CCN} = N_{amb} \cdot A_{CCN}. \qquad (10)$$

**Table 3.** CCN Concentrations N$_{CCN}$ (cm$^{-3}$) and Activated Fraction $A_{CCN}$ of the Total Ambient Aerosol $N_{amb}$ (cm$^{-3}$) for Zurich (April 2010) in the Size Range of $d = 10$–1000 nm From ECHAM6-HAM2 for Typical Ambient Supersaturations SS

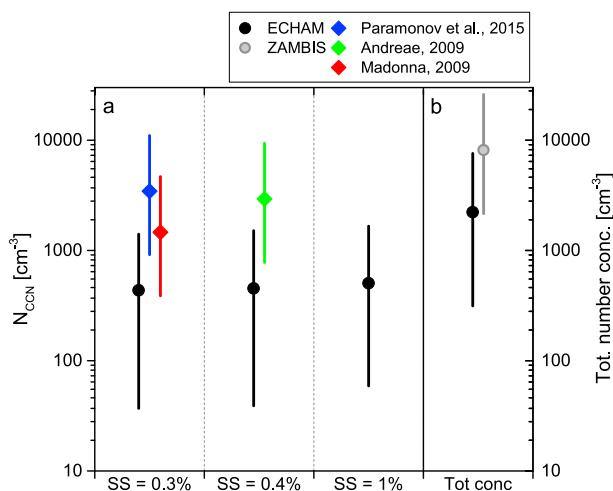| SS (%) | Mean $N_{CCN}$ (cm$^{-3}$) | Minimum to Maximum $N_{CCN}$ (cm$^{-3}$) | $A_{CCN}$ |
| --- | --- | --- | --- |
| 0.3 | 434 ± 246 | 37–1406 | 0.21 ± 0.08 |
| 0.4 | 451 ± 262 | 39–1511 | 0.22 ± 0.08 |
| 1.0 | 503 ± 289 | 59–1663 | 0.24 ± 0.10 |
| Total | 2220 ± 1404 | 314–7567 | |

**Figure 11.** (a) CCN concentrations ($N_{CCN}$) predicted for a global average (global) [*Paramonov et al.*, 2015], for polluted continental aerosol (poll) [*Andreae*, 2009], and for a polluted urban location (ZH) [*Madonna*, 2009] are given in colors, and the CCN concentration taken from ECHAM6-HAM2 is shown in black. (b) The total aerosol number concentrations from ECHAM6-HAM2 (black) and measured aerosol number concentration during ZAMBIS ($N_{amb}$, grey) are shown. Points indicate mean values and bars the range of concentrations.

The resulting CCN concentrations for the three cases are given in Table 2. A comparison of the three CCN estimations to typical aerosol properties obtained with the ECHAM6-HAM2 global aerosol-climate model is presented for model specifications in *Neubauer et al.* [2014] to identify which estimation for CCN describes measurements during ZAMBIS the best. $N_{CCN,ECHAM}$ (Table 3) is calculated for the surface aerosol in spring in Zurich (3 h instantaneous data for April 2010, interpolated to the coordinates of Zurich) and representative for the typical aerosol size distribution, number, and composition as can be expected during ZAMBIS. $N_{CCN,ECHAM}$ is on average $434 \pm 246 \, \text{cm}^{-3}$ at $SS = 0.3\%$ ($451 \pm 262 \, \text{cm}^{-3}$ at $SS = 0.4\%$) corresponding to $A_{CCN,ECHAM} = 0.21 \pm 0.08$ ($0.22 \pm 0.08$ at $SS = 0.4\%$). $N_{CCN}$ from the three estimations discussed above including the total aerosol number concentration from ECHAM6-HAM2 and the measured $N_{amb}$ during ZAMBIS are shown in Figure 11. At $SS = 0.3\%$ and $SS = 0.4\%$, estimated mean $N_{CCN}$ are significantly higher than $N_{CCN,ECHAM}$ (factor $3.4 - 7.9$ for $SS = 0.3\%$ and factor 6.5 for $SS = 0.4\%$). $N_{amb}$ is $2.2 \cdot 10^3 \, \text{cm}^{-3}$ to $2.6 \cdot 10^4 \, \text{cm}^{-3}$ for the investigated size range of $10 - 880$ nm (Figure 11b, grey). A discrepancy between the measured and the modeled total number concentration obtained from ECHAM6-HAM2 for a comparable size range of ambient aerosol is found to be a factor of 3.7 (Figure 11b). This indicates that the local number concentration of the ambient aerosol during ZAMBIS is underestimated by the model output from ECHAM6-HAM2 for the surface aerosol. This could be due to local influences at the site, e.g., pollution from traffic or wood fires. However, the discrepancies between $N_{CCN,ECHAM}$ and the three cases for $N_{CCN}$ are significantly larger. Best agreement is found for $N_{CCN,ZH}$ (factor 3.4 for $SS = 0.3\%$), which suggests that the aerosol measured during ZAMBIS is best described by an urban aerosol measured in the same area by *Madonna* [2009].
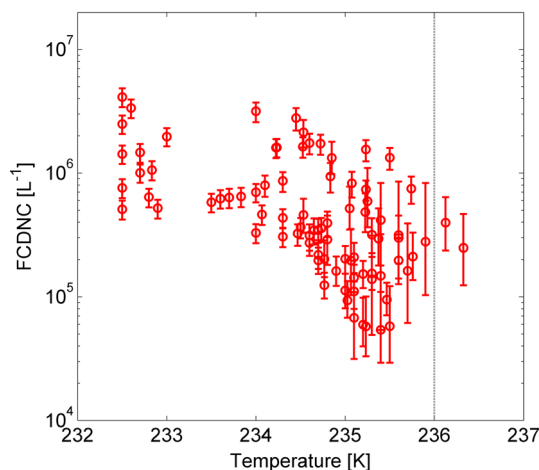


**Figure 12.** FCDNC for aerosol number concentrations predicted for CCN activation based on a study at an urban location for $SS = 0.3\%$ [*Madonna*, 2009]. The vertical dashed line separates homogeneous and heterogeneous freezing regimes in PIMCA-PINC.

$N_{CCN}$ only represents estimations for the surface aerosol. Typically, cloud droplet number concentrations in the atmosphere at altitudes relevant for ice nucleation may be significantly lower due to sedimentation and scavenging of the surface aerosol. Therefore, we suggest these numbers used for following calculations to be an upper limit for available cloud droplet numbers in the atmosphere where ice nucleation takes place via immersion freezing.

The frozen cloud droplet number concentration (FCDNC), which is the fraction of cloud droplets that can potentially freeze, is given as

$$FCDNC(T) = FF_{adjtot}(T) \cdot N_{amb} \cdot A_{CCN,ZH}, \quad (11)$$

where $FF_{adjtot}$ is taken from Figure 8b. The resulting FCDNC as a function of $T$ is given in Figure 12 with FCDNC between $5.4 \cdot 10^4$ and $4.1 \cdot 10^6 \, \text{L}^{-1}$

(mean FCDNC = $7.22 \cdot 10^5$ L$^{-1}$, SS = 0.3%). These values are only calculated for FF$_{adjtot}$ > 0.1. The measurement uncertainties given as error bars are discussed in Appendix A.

The FCDNC presented gives the number of available cloud droplets in the atmosphere which are based on ground level CCN activation for conditions in the polluted boundary layer. Freezing of the droplets is measured with PIMCA-PINC as a frozen fraction during ZAMBIS and applied to the available number of cloud droplets. Therefore, FCDNC can be seen as an upper limit of cloud droplets in the atmosphere at altitudes where immersion freezing can occur. We note that most measurements were performed at temperatures dominated by homogeneous freezing. Therefore, an aerosol particle is only required for the CCN activation but not for homogeneous freezing at temperatures $T < 236$ K in PIMCA-PINC.

Most experiments during ZAMBIS showed FF$_{adjtot}$ < 0.1 for temperatures $T > 236$ K, where ice primarily forms due to heterogeneous ice nucleation. The exception was the first week of April, when heterogeneous freezing for $T > 236$ K was measured. For comparison with previous studies on ambient observations of INPs, the INP concentrations for measurements during ZAMBIS is predicted based on the parameterization by *DeMott et al.* [2010] (hereafter: D10). They found a good correlation between the INP concentration and the measured ambient particle concentrations for sizes larger 0.5 μm based on a comprehensive data set from airborne and ground-based experiments measured with a CFDC above water saturation. According to equation (1) by *DeMott et al.* [2010] and the measured $N_{amb > 0.5\mu m}$ (cm$^{-3}$) during ZAMBIS, the INP$_{D10}$ is $54 \pm 39$ L$^{-1}$ at $T = 238$ K. This is the coldest temperature the parameterization is valid for and does not cover the temperature range where heterogeneous ice nucleation was observed during ZAMBIS. Concentrations summarized from observations in *DeMott et al.* [2010] range from 0.01 stdL$^{-1}$ to 400 stdL$^{-1}$ for temperatures 238–264 K. Because measurements during ZAMBIS were obtained at $T < 238$ K a direct comparison of the FCDNC to INP concentrations by *DeMott et al.* [2010] is therefore not applicable as a change in temperature by 2 K could result in a significantly higher ice nucleation activity. The FCDNC (mean $7.22 \cdot 10^5$ L$^{-1}$ for $T < 238$ K) and INP$_{D10}$ ($54 \pm 39$ L$^{-1}$ at $T < 238$ K) give the upper and lower limit possible for INP concentrations in this atmosphere in this temperature regime that would be possible from measurements with PIMCA-PINC during ZAMBIS.

The calculation presented here only considers aerosol particles larger than 0.5 μm for the INP concentration. In addition, the INP concentration in this work was only derived for the submicron size range of the atmospheric aerosol size distribution (cf. Appendix C). *Mason et al.* [2016] reported size-resolved INPs measurements for various ground sites. They found about 40–95% of the observed INP being larger than 1 μm and 20–65% larger than 2.5 μm at 248 K. This suggests that supermicron and coarse-mode particles are a significant fraction of the INP population. In summary this could result in underestimating INP$_{D10}$ concentration, because we neither sampled supermicron particles nor considered aerosol particles smaller than 0.5 μm in the derivation of INP$_{D10}$. Compared to previous studies on immersion mode INPs, the investigated temperatures during ZAMBIS are close to the homogeneous freezing regime making it difficult to directly compare to other immersion freezing measurements which are reported for $T \gg 236$ K [e.g., *Conen et al.*, 2012, 2015; *Hader et al.*, 2014; *Mason et al.*, 2015b].

In summary, the calculation of the INP concentration from measurements of frozen fraction is difficult, as assumptions have to be made when referring to aerosol numbers and sizes sampled. In offline methods this is not crucial as such methods refer to the most ice nucleation active aerosol particle per sample unit. Because the sample volumes in offline methods contain polydisperse aerosol particles, activation already occurs at warmer temperatures compared to single-immersed methods.

## 5. Conclusions and Outlook

In this work we introduced the portable immersion freezing instrument, PIMCA, for online measurements of single-immersed aerosol particles. PIMCA extends PINC vertically and is controlled independently from PINC. PIMCA-PINC can be deployed in the field and remote laboratories. Sample temperatures as low as 233 K can be reached to obtain the freezing behavior of the sample aerosol as a frozen fraction (FF). The design is based on the laboratory instrument IMCA-ZINC [*Lüönd et al.*, 2010] but has been adapted based on the constraints of a portable setup. Particle detection and discrimination between ice crystals and cloud droplets is achieved by measuring the depolarization intensity of plane polarized light and leads to FF as a function of temperature. The most important changes are a thermoelectric, Peltier-module-based cooling system without the requirement of a cooling liquid and a reduced total sample/sheath flow rate. The new total flow rate of 5 lpm in the PIMCA-PINC setup leads to cloud droplets with a radius of 5–7 μm which have an ice nucleation time

of ~7 s. Homogeneous freezing experiments were used to validate the freezing conditions in PIMCA-PINC. Immersion freezing experiments of size-selected kaolinite particles agree well with previously published data measured with IMCA-ZINC but exceed FFs of measurements reported by *Hartmann et al.* [2016]. The reasons for the discrepancy are likely due to longer residence times and possibly larger effective particle sizes in the current work leading to a larger particle surface area available for ice nucleation. Simultaneous measurements to compare different immersion freezing experiments, such as LACIS and the portable PIMCA-PINC, will help to confirm the influence of particle size selection and residence time.

Ambient in situ experiments were conducted during the ZAMBIS campaign in spring 2014 at an urban-forest site in Zurich, Switzerland. Due to the polydisperse aerosol with a large fraction of small aerosol particles, it was necessary to account for undetected aerosol particles during the experiments leading to an adjusted frozen fraction ($FF_{adjtot}$). Experiments from a period of about 6 weeks resulted in data with the majority of experiments in the temperature regime where homogeneous freezing is expected to dominate. Yet a smaller fraction of heterogeneous freezing which is not quantifiable by the PIMCA-PINC sensitivities in the current state is possible for the measured atmospheric aerosol.

The cloud condensation nuclei (CCN) concentration was estimated to predict the available number of cloud droplets for immersion freezing in the atmosphere. CCN activated fractions for urban aerosol measured in the city of Zurich ($A_{CCN,ZH}$) by *Madonna* [2009] agreed best to aerosol properties during ZAMBIS. They were chosen by comparison to aerosol data from ECHAM6-HAM2. By applying the measured frozen fraction to the available CCN, the FCDNC was obtained. The FCDNC is an upper limit of ice crystals which can be formed in the atmosphere based on the primary ice nucleation processes of homogeneous nucleation and immersion freezing for $T < 238$ K. In the heterogeneous freezing regime, the parameterization by *DeMott et al.* [2010] was used to estimate the INP concentration at $T = 238$ K. With the mean observed aerosol number concentration larger 0.5 μm during ZAMBIS, $INP_{D10}$ is $54 \pm 39$ L$^{-1}$ at $T = 238$ K. We suggest this as a lower limit for the investigated temperatures in an urban environment.

At the present state the PIMCA-PINC setup can be used for laboratory studies and instrument intercomparison [e.g., *Hiranuma et al.*, 2015; *Wex et al.*, 2015] as it is the only portable instrument to measure immersion freezing of single-immersed aerosol particles that excludes other ice nucleation mechanisms. To study ambient immersion freezing in a broader temperature regime more relevant for mixed-phase clouds, the detection limit has to be lowered. Ambient ice nucleation experiments on size-selected single-immersed aerosol particles can be used if these are available in sufficiently large concentrations. Similar studies have been presented recently for droplet freezing studies on dilute solution droplets [e.g., *Hader et al.*, 2014; *Mason et al.*, 2016] but not yet for individual aerosol particles. Conducting field studies with size-selected particles would reduce the challenge of small aerosol particles activating into droplets in PIMCA causing a FF below the detection limit of the current experiment. Additionally, size resolved information on the chemical composition of the ambient aerosol particles would be helpful to better understand which components predominantly act as INPs.

A reduction in the uncertainty from particle misclassification in IODE would be possible in an experimental setup without the evaporation section to increase the signal intensity by keeping droplets at a larger size. This could be achieved when IODE is positioned in the main ice nucleation chamber or if the evaporation section can be used as an extended main chamber. For both options major changes in the cooling circuitry of PINC would be necessary. Furthermore, a chamber without an evaporation section would allow the use of a more sensitive detector to distinguish the particle phase downstream of PINC. This will be addressed in future developments of PIMCA-PINC. For future analysis of aerosol particles, sampling of ice residuals could be achieved via isolation of large ice crystals through a device such as a Pumped-Counterflow Virtual Impactor (P-CVI) [*Kulkarni et al.*, 2011] coupled downstream of PIMCA-PINC. Ice crystals separated by a P-CVI could be collected onto substrates for further analysis. After sublimation of the ice crystals, the residuals can be analyzed, for example, via scanning electron microscopy with energy-dispersive X-ray (SEM-EDX) microanalysis in order to obtain information about their composition [*Worringen et al.*, 2015].

## Appendix A: Evaluation of Measurement Uncertainties for PIMCA-PINC Experiments

The applied temperature gradient between the chamber walls of PINC leads to a supersaturation profile in the chamber. Validation experiments for PINC by *Chou et al.* [2011] showed a resulting uncertainty in RH of $\pm 2\%$ based on ammonium sulfate studies on deliquescence [*Kanji and Abbatt*, 2006; *Braban et al.*, 2001] and
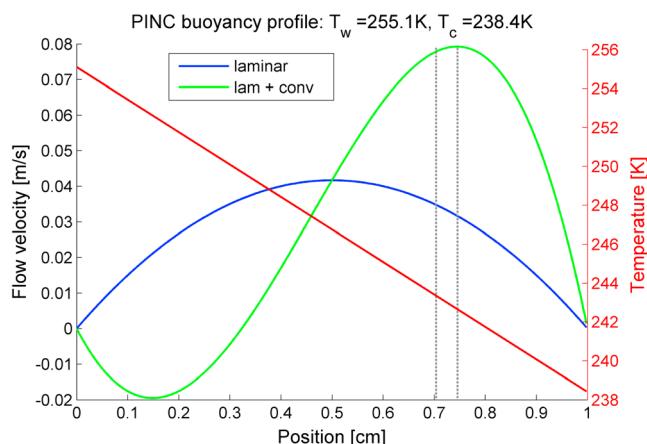
**Figure A1.** Typical flow profile for PINC at a total flow rate of 5 lpm and a target temperature of 243 K at water saturation. The red line indicates the temperature between the chamber walls (position 0 cm is the warm wall, position 1 cm is the cold wall). The laminar flow profile is shown in blue and in green the buoyant flow (takes into account convection). In comparison to the laminar flow, consideration of buoyancy shifts the sample lamina (grey lines) toward the colder chamber walls according to the maximum flow velocity.

homogeneous freezing (based on theoretical calculations by *Koop et al.* [2000]). The uncertainty of the thermocouples measuring the temperature at different positions along the chamber is $\pm 0.1$ K. The variation of temperature in the sample layer was estimated to be 0.8 K [*Kanji et al.*, 2013]. The velocity profile and the sample position in PIMCA-PINC is calculated for the flow rate of 2.2 lpm of sheath air on each side and a sample flow of 0.6 lpm. Consideration of convective forces due to the temperature gradient results in a shift of the sample layer closer to the colder chamber wall. Figure A1 shows the shift in the sample position, the flow velocities, and the linear temperature gradient between the warm wall (position: 0 cm) and the cold wall (position: 1 cm) in PINC. The position of the sample layer is indicated as dash-dotted lines located at a position of 2.5–3 mm from the cold wall for $T = 242.7$ K at $RH_w = 101\%$ (equivalent to $RH_w \geq 100\%$ throughout the whole sample layer). The flow profile and the position of the sample layer depend on set points of ice nucleation temperature and $RH_w$. The corresponding saturation profile is shown in Figure A2.

Error bars in FCDNC (Figure 12) arise from error propagation based on the measurement uncertainty for size distribution data of 10% and the reported uncertainty obtained from $FF_{adjtot}$ (cf. section 2.3). In addition, the uncertainty in $A_{CCN,ZH}$ is considered in the error propagation for the calculation of FCDNC.
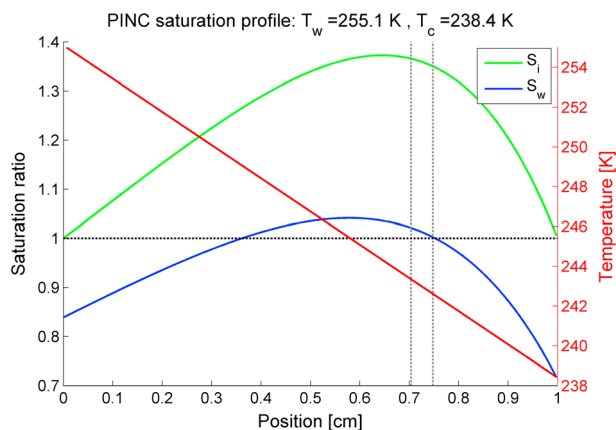


**Figure A2.** Typical saturation profile for PINC with respect to ice ($S_i$) and water ($S_w$) at a total flow rate of 5 lpm and a target temperature of 243 K. Temperature conditions in the chamber cross section are shown in red. The position of the sample layer is indicated with grey vertical lines.
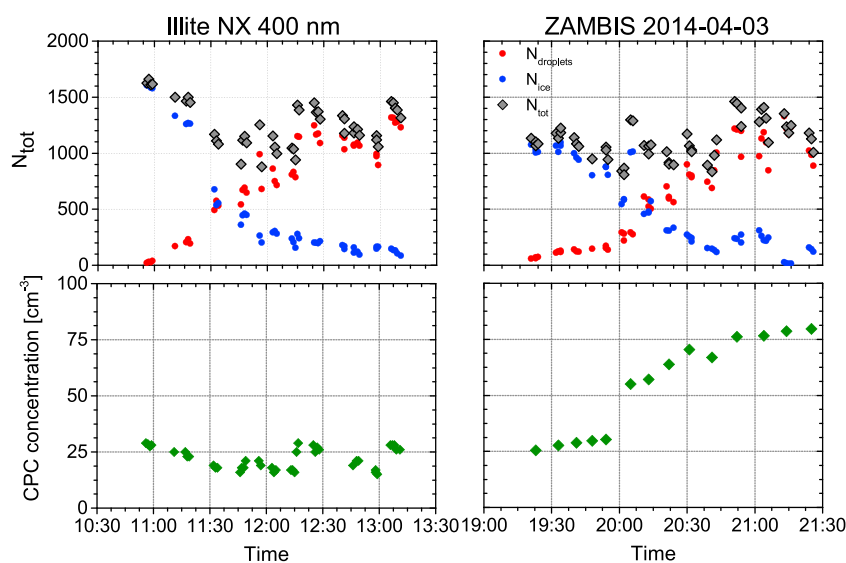
**Figure B1.** Ice crystal and cloud droplet numbers detected by IODE during individual, 35 s experiments with parallel measurements of aerosol number concentration after the dilution stage (lower panels). The left column shows measurements of size-selected 400 nm illite particles. The right column shows data from a field case with polydisperse particles during ZAMBIS.

## Appendix B: Particle Activation in PIMCA-PINC

As discussed in section 4.2, a correction for the activation of particles in PIMCA-PINC is applied. In Figure B1 particle activation is compared for two studies. The case of size-selected 400 nm illite particles is compared to the field case of 3 April 2014 during ZAMBIS. Particle counts per measurement of ice crystals, droplets, and total counts of IODE are shown in the top row in Figure B1 and the particle concentration measured upstream of PIMCA-PINC in the bottom row in Figure B1. The case of size-selected 400 nm particles is compared to the field case of 3 April during ZAMBIS. Particle concentrations are controlled by a dilution system to prevent coincidence in the detector. The experimental temperatures of the data shown increased with time, which leads to a decrease in ice and an increase in the liquid droplet fraction. In the illite experiment the total IODE counts remain constant while the aerosol particle concentration was held between 15 and 30 cm$^{-3}$. During the field study to find a constant number of detected particles in IODE, the sampled aerosol concentration had to be increased as higher experimental temperatures were accessed. This indicates that polydisperse particles sampled from the ambient were not always detectable as cloud droplets at the position of IODE due to smaller droplet sizes and evaporation before the detector. This behavior is not found for size-selected aerosol.

## Appendix C: Particle Losses in the Aerosol Inlet System

Particle losses were considered between the sample inlet and the PIMCA-PINC setup. A total flow rate 1.6 lpm was used in a 6 mm tube with an approximate length of 5 m consisting mostly of a horizontal sample line and some 90° bends. Particle loss calculations showed losses of 10% for 1 μm particles and 50% loss for particles $d > 2$ μm. Considering the ambient size distribution and that the large majority of the particles have diameters <1 μm, it can be assumed that a possible depolarization signal arising from unactivated large aerosol particles is negligible.

For measurements of the ambient aerosol size distributions, the SMPS sample line was positioned on a separate, however, identical inlet positioned 1.5 m from the PIMCA-PINC inlet on the measurement trailer. A total flow rate of 2 lpm and nearly vertical tubing of about 1.5 m result in a particle loss smaller than 0.5% for the entire aerosol size distribution and for aerosol diameters <1 μm even smaller (less than 0.02%).

## References

Abbatt, J. P. D., S. Benz, D. J. Cziczo, Z. Kanji, U. Lohmann, and O. Möhler (2006), Solid ammonium sulfate aerosols as ice nuclei: A pathway for cirrus cloud formation, *Science*, *313*(5794), 1770–1773, doi:10.1126/science.1129726.

Andreae, M. O. (2009), Correlation between cloud condensation nuclei concentration and aerosol optical thickness in remote and polluted regions, *Atmos. Chem. Phys.*, *9*(2), 543–556, doi:10.5194/acp-9-543-2009.

Ansmann, A., H. Baars, M. Tesche, D. Müller, D. Althausen, R. Engelmann, T. Pauliquevis, and P. Artaxo (2009), Dust and smoke transport from Africa to South America: Lidar profiling over Cape Verde and the Amazon rainforest, *Geophys. Res. Lett.*, *36*, L11802, doi:10.1029/2009GL037923.

ANSYS (2011), *ANSYS FLUENT User's Guide, Release Version 14.0*, ANSYS, Canonsburg, Pa.

Ardon-Dryer, K., and Z. Levin (2014), Ground-based measurements of immersion freezing in the eastern Mediterranean, *Atmos. Chem. Phys.*, *14*(10), 5217–5231, doi:10.5194/acp-14-5217-2014.

Augustin-Bauditz, S., H. Wex, S. Kanter, M. Ebert, D. Niedermeier, F. Stolz, A. Prager, and F. Stratmann (2014), The immersion mode ice nucleation behavior of mineral dusts: A comparison of different pure and surface modified dusts, *Geophys. Res. Lett.*, *41*, 7375–7382, doi:10.1002/2014GL061317.

Bigg, E. K. (1967), Cross sections of ice nucleus concentrations at altitude over long paths, *J. Atmos. Sci.*, *24*(2), 226–229, doi:10.1175/1520-0469(1967)024<0226:CSOINC>2.0.CO;2.

Boose, Y., et al. (2016), Ice nucleating particle measurements at 241 K during winter months at 3580 m a.s.l. in the Swiss Alps, *J. Atmos. Sci.*, doi:10.1175/JAS-D-15-0236.1, in press.

Braban, C. F., J. P. D. Abbatt, and D. J. Cziczo (2001), Deliquescence of ammonium sulfate particles at sub-eutectic temperatures, *Geophys. Res. Lett.*, *28*(20), 3879–3882, doi:10.1029/2001GL013175.

Chou, C., O. Stetzer, E. Weingartner, Z. Jurányi, Z. A. Kanji, and U. Lohmann (2011), Ice nuclei properties within a Saharan dust event at the Jungfraujoch in the Swiss Alps, *Atmos. Chem. Phys.*, *11*(10), 4725–4738, doi:10.5194/acp-11-4725-2011.

Conen, F., S. Henne, C. E. Morris, and C. Alewell (2012), Atmospheric ice nucleators active ≥−12°C can be quantified on PM$_{10}$ filters, *Atmos. Meas. Tech.*, *5*(2), 321–327, doi:10.5194/amt-5-321-2012.

Conen, F., S. Rodríguez, C. Hüglin, S. Henne, E. Herrmann, N. Bukowiecki, and C. Alewell (2015), Atmospheric ice nuclei at the high-altitude observatory Jungfraujoch, Switzerland, *Tellus B*, *67*, 25014, doi:10.3402/tellusb.v67.25014.

Connolly, P. J., C. Emersic, and P. R. Field (2012), A laboratory investigation into the aggregation efficiency of small ice crystals, *Atmos. Chem. Phys.*, *12*(4), 2055–2076, doi:10.5194/acp-12-2055-2012.

Cziczo, D. J., K. D. Froyd, C. Hoose, E. J. Jensen, M. Diao, M. A. Zondlo, J. B. Smith, C. H. Twohy, and D. M. Murphy (2013), Clarifying the dominant sources and mechanisms of cirrus cloud formation, *Science*, *340*(6138), 1320–1324, doi:10.1126/science.1234145.

DeMott, P. J., A. J. Prenni, X. Liu, S. M. Kreidenweis, M. D. Petters, C. H. Twohy, M. S. Richardson, T. Eidhammer, and D. C. Rogers (2010), Predicting global atmospheric ice nuclei distributions and their impacts on climate, *Proc. Natl. Acad. Sci. U.S.A.*, *107*(25), 11,217–11,222, doi:10.1073/pnas.0910818107.

Ditas, F., R. A. Shaw, H. Siebert, M. Simmel, B. Wehner, and A. Wiedensohler (2012), Aerosols-cloud microphysics-thermodynamics-turbulence: Evaluating supersaturation in a marine stratocumulus cloud, *Atmos. Chem. Phys.*, *12*(5), 2459–2468, doi:10.5194/acp-12-2459-2012.

Earle, M. E., T. Kuhn, A. F. Khalizov, and J. J. Sloan (2010), Volume nucleation rates for homogeneous freezing in supercooled water microdroplets: Results from a combined experimental and modelling approach, *Atmos. Chem. Phys.*, *10*(16), 7945–7961, doi:10.5194/acp-10-7945-2010.

Hader, J. D., T. P. Wright, and M. D. Petters (2014), Contribution of pollen to atmospheric ice nuclei concentrations, *Atmos. Chem. Phys.*, *14*(11), 5433–5449, doi:10.5194/acp-14-5433-2014.

Hammer, E., N. Bukowiecki, M. Gysel, Z. Jurányi, C. R. Hoyle, R. Vogt, U. Baltensperger, and E. Weingartner (2014), Investigation of the effective peak supersaturation for liquid-phase clouds at the high-alpine site Jungfraujoch, Switzerland (3580 m a.s.l.), *Atmos. Chem. Phys.*, *14*(2), 1123–1139, doi:10.5194/acp-14-1123-2014.

Hartmann, S., D. Niedermeier, J. Voigtländer, T. Clauss, R. A. Shaw, H. Wex, A. Kiselev, and F. Stratmann (2011), Homogeneous and heterogeneous ice nucleation at LACIS: Operating principle and theoretical studies, *Atmos. Chem. Phys.*, *11*(4), 1753–1767, doi:10.5194/acp-11-1753-2011.

Hartmann, S., H. Wex, T. Clauss, S. Augustin-Bauditz, D. Niedermeier, M. Rösch, and F. Stratmann (2016), Immersion freezing of kaolinite: Scaling with particle surface area, *J. Atmos. Sci.*, *73*(1), 263–278, doi:10.1175/JAS-D-15-0057.1.

Hiranuma, N., et al. (2015), A comprehensive laboratory study on the immersion freezing behavior of illite NX particles: A comparison of 17 ice nucleation measurement techniques, *Atmos. Chem. Phys.*, *15*(5), 2489–2518, doi:10.5194/acp-15-2489-2015.

Hudson, J. G., and S. Noble (2013), CCN and vertical velocity influences on droplet concentrations and supersaturations in clean and polluted stratus clouds, *J. Atmos. Sci.*, *71*(1), 312–331, doi:10.1175/JAS-D-13-086.1.

Joly, M., P. Amato, L. Deguillaume, M. Monier, C. Hoose, and A.-M. Delort (2014), Quantification of ice nuclei active at near 0°C temperatures in low-altitude clouds at the Puy de Dôme atmospheric station, *Atmos. Chem. Phys.*, *14*(15), 8185–8195, doi:10.5194/acp-14-8185-2014.

Kanji, Z. A., and J. P. D. Abbatt (2006), Laboratory studies of ice formation via deposition mode nucleation onto mineral dust and n-hexane soot samples, *J. Geophys. Res.*, *111*, D16204, doi:10.1029/2005JD006766.

Kanji, Z. A., and J. P. D. Abbatt (2009), The University of Toronto Continuous Flow Diffusion Chamber (UT-CFDC): A simple design for ice nucleation studies, *Aerosol Sci. Technol.*, *43*(7), 730–738, doi:10.1080/02786820902889861.

Kanji, Z. A., A. Welti, C. Chou, O. Stetzer, and U. Lohmann (2013), Laboratory studies of immersion and deposition mode ice nucleation of ozone aged mineral dust particles, *Atmos. Chem. Phys.*, *13*(17), 9097–9118, doi:10.5194/acp-13-9097-2013.

Klein, H., et al. (2010), Saharan dust and ice nuclei over Central Europe, *Atmos. Chem. Phys.*, *10*(21), 10,211–10,221, doi:10.5194/acp-10-10211-2010.

Koop, T., B. Luo, A. Tsias, and T. Peter (2000), Water activity as the determinant for homogeneous ice nucleation in aqueous solutions, *Nature*, *406*(6796), 611–614, doi:10.1038/35020537.

Kulkarni, G., M. Pekour, A. Afchine, D. M. Murphy, and D. J. Cziczo (2011), Comparison of experimental and numerical studies of the performance characteristics of a pumped counterflow virtual impactor, *Aerosol Sci. Technol.*, *45*(3), 382–392, doi:10.1080/02786826.2010.539291.

Lohmann, U., and J. Feichter (2005), Global indirect aerosol effects: A review, *Atmos. Chem. Phys.*, *5*(3), 715–737, doi:10.5194/acp-5-715-2005.

Lüönd, F., O. Stetzer, A. Welti, and U. Lohmann (2010), Experimental study on the ice nucleation ability of size-selected kaolinite particles in the immersion mode, *J. Geophys. Res.*, *115*, D14201, doi:10.1029/2009JD012959.

Madonna, E. (2009), Cloud condensation nuclei measurements of urban aerosols, Zürich, Switzerland.

Marcolli, C. (2014), Deposition nucleation viewed as homogeneous or immersion freezing in pores and cavities, *Atmos. Chem. Phys.*, *14*(4), 2071–2104, doi:10.5194/acp-14-2071-2014.

Mason, R. H., C. Chou, C. S. McCluskey, E. J. T. Levin, C. L. Schiller, T. C. J. Hill, J. A. Huffman, P. J. DeMott, and A. K. Bertram (2015a), The micro-orifice uniform deposit impactor-droplet freezing technique (MOUDI-DFT) for measuring concentrations of ice nucleating particles as a function of size: Improvements and initial validation, *Atmos. Meas. Tech.*, *8*(6), 2449–2462, doi:10.5194/amt-8-2449-2015.

Mason, R. H., et al. (2015b), Ice nucleating particles at a coastal marine boundary layer site: Correlations with aerosol type and meteorological conditions, *Atmos. Chem. Phys.*, *15*(21), 12,547–12,566, doi:10.5194/acp-15-12547-2015.

Mason, R. H., et al. (2016), Size-resolved measurements of ice-nucleating particles at six locations in North America and one in Europe, *Atmos. Chem. Phys.*, *16*(3), 1637–1651, doi:10.5194/acp-16-1637-2016.

Murray, B. J., et al. (2010), Heterogeneous nucleation of ice particles on glassy aerosols under cirrus conditions, *Nat. Geosci.*, *3*(4), 233–237.

Murray, B. J., D. O'Sullivan, J. D. Atkinson, and M. E. Webb (2012), Ice nucleation by particles immersed in supercooled cloud droplets, *Chem. Soc. Rev.*, *41*(19), 6519–6554, doi:10.1039/C2CS35200A.

Neubauer, D., U. Lohmann, C. Hoose, and M. G. Frontoso (2014), Impact of the representation of marine stratocumulus clouds on the anthropogenic aerosol effect, *Atmos. Chem. Phys.*, *14*(21), 11,997–12,022, doi:10.5194/acp-14-11997-2014.

Nicolet, M., O. Stetzer, F. Lüönd, O. Möhler, and U. Lohmann (2010), Single ice crystal measurements during nucleation experiments with the depolarization detector IODE, *Atmos. Chem. Phys.*, *10*(2), 313–325, doi:10.5194/acp-10-313-2010.

Niedermeier, D., et al. (2010), Heterogeneous freezing of droplets with immersed mineral dust particles–Measurements and parameterization, *Atmos. Chem. Phys.*, *10*(8), 3601–3614, doi:10.5194/acp-10-3601-2010.

Niemand, M., et al. (2012), A particle-surface-area-based parameterization of immersion freezing on desert dust particles, *J. Atmos. Sci.*, *69*(10), 3077–3092, doi:10.1175/JAS-D-11-0249.1.

Paramonov, M., et al. (2015), A synthesis of cloud condensation nuclei counter (CCNC) measurements within the EUCAARI network, *Atmos. Chem. Phys.*, *15*(21), 12,211–12,229, doi:10.5194/acp-15-12211-2015.

Phillips, V. T. J., L. J. Donner, and S. T. Garner (2007), Nucleation processes in deep convection simulated by a cloud-system-resolving model with double-moment bulk microphysics, *J. Atmos. Sci.*, *64*(3), 738–761, doi:10.1175/JAS3869.1.

Pruppacher, H., and J. Klett (1997), *Microphysics of Clouds and Precipitation, Atmos. and Oceanogr. Sci. Lib.*, Kluwer Acad., Dordrecht, London.

Rogers, D. C. (1988), Development of a continuous flow thermal gradient diffusion chamber for ice nucleation studies, *Atmos. Res.*, *22*(2), 149–181, doi:10.1016/0169-8095(88)90005-1.

Rogers, D. C., P. J. DeMott, S. M. Kreidenweis, and Y. Chen (1998), Measurements of ice nucleating aerosols during SUCCESS, *Geophys. Res. Lett.*, *25*(9), 1383–1386, doi:10.1029/97GL03478.

Seinfeld, J. H., and S. N. Pandis (2006), *Atmospheric Chemistry and Physics: From Air Pollution to Climate Change*, 2nd ed., John Wiley, Hoboken, N. J.

Stetzer, O., B. Baschek, F. Lüönd, and U. Lohmann (2008), The Zurich ice nucleation chamber ZINC–A new instrument to investigate atmospheric ice formation, *Aerosol Sci. Technol.*, *42*(1), 64–74, doi:10.1080/02786820701787944.

Stopelli, E., F. Conen, L. Zimmermann, C. Alewell, and C. E. Morris (2014), Freezing nucleation apparatus puts new slant on study of biological ice nucleators in precipitation, *Atmos. Meas. Tech.*, *7*(1), 129–134, doi:10.5194/amt-7-129-2014.

Stratmann, F., A. Kiselev, S. Wurzler, M. Wendisch, J. Heintzenberg, R. J. Charlson, K. Diehl, H. Wex, and S. Schmidt (2004), Laboratory studies and numerical simulations of cloud droplet formation under realistic supersaturation conditions, *J. Atmos. Oceanic Technol.*, *21*(6), 876–887, doi:10.1175/1520-0426(2004)021<0876:LSANSO>2.0.CO;2.

Vali, G. (1985), Nucleation terminology, *J. Aerosol Sci.*, *16*(6), 575–576, doi:10.1016/0021-8502(85)90009-6.

Vali, G., P. J. DeMott, O. Möhler, and T. F. Whale (2015), Technical note: A proposal for ice nucleation terminology, *Atmos. Chem. Phys.*, *15*(18), 10,263–10,270, doi:10.5194/acp-15-10263-2015.

Welti, A., F. Lüönd, Z. A. Kanji, O. Stetzer, and U. Lohmann (2012), Time dependence of immersion freezing: An experimental study on size selected kaolinite particles, *Atmos. Chem. Phys.*, *12*(20), 9893–9907, doi:10.5194/acp-12-9893-2012.

Westbrook, C. D., and A. J. Illingworth (2011), Evidence that ice forms primarily in supercooled liquid clouds at temperatures $>-27°$C, *Geophys. Res. Lett.*, *38*, L14808, doi:10.1029/2011GL048021.

Wex, H., P. J. DeMott, Y. Tobo, S. Hartmann, M. Rösch, T. Clauss, L. Tomsche, D. Niedermeier, and F. Stratmann (2014), Kaolinite particles as ice nuclei: Learning from the use of different kaolinite samples and different coatings, *Atmos. Chem. Phys.*, *14*(11), 5529–5546, doi:10.5194/acp-14-5529-2014.

Wex, H., et al. (2015), Intercomparing different devices for the investigation of ice nucleating particles using Snomax as test substance, *Atmos. Chem. Phys.*, *15*(3), 1463–1485, doi:10.5194/acp-15-1463-2015.

Wiedensohler, A., et al. (2012), Mobility particle size spectrometers: Harmonization of technical standards and data structure to facilitate high quality long-term observations of atmospheric particle number size distributions, *Atmos. Meas. Tech.*, *5*(3), 657–685, doi:10.5194/amt-5-657-2012.

Worringen, A., et al. (2015), Single-particle characterization of ice-nucleating particles and ice particle residuals sampled by three different techniques, *Atmos. Chem. Phys.*, *15*(8), 4161–4178, doi:10.5194/acp-15-4161-2015.

Wright, T. P., J. D. Hader, G. R. McMeeking, and M. D. Petters (2014), High relative humidity as a trigger for widespread release of ice nuclei, *Aerosol Sci. Technol.*, *48*(11), 1–5, doi:10.1080/02786826.2014.968244.